Experimental and Theoretical Study of Hyperfine WDM Demultiplexer Performance Using the Virtually Imaged Phased-Array (VIPA)

Shijun Xiao, *Student Member, IEEE, Student Member, OSA*, Andrew M. Weiner, *Fellow, IEEE*, and Christopher Lin

***Abstract*—We have developed a Fresnel diffraction analysis that provides an analytic expression for the passband response of virtually imaged phased-array (VIPA) demultiplexers. Our analysis shows that although the passband can be inherently symmetric, a strong asymmetry can develop when the output plane is detuned longitudinally. The symmetric passband has the minimum −3 dB transmission bandwidth. We also identify a spatial chirp effect that arises when the passband becomes asymmetric. Our theoretical predictions are confirmed via experiment. The experimental results include a demonstration of a hyperfine wavelength demultiplexing response with 10 pm (1.25 GHz) −3 dB transmission bandwidth.**

***Index Terms*—Optical devices, spectral dispersers, wavelength demultiplexers.**

I. Introduction

TECHNOLOGY for separating and combining wavelengths is fundamental to wavelength-division multiplexing (WDM). Multiplexing-demultiplexing devices with substantially finer spectral resolution could lead to new opportunities for networks with finer wavelength granularity and larger channel counts, as well as new possibilities for optical signal processing. The arrayed waveguide grating (AWG) is a highly developed technology, but currently the 3-dB bandwidth is limited to 4 GHz in 10-GHz channel spacing [1]. Technology based on a modified, side-entrance Fabry–Pérot etalon termed a virtually imaged phased-array (VIPA) [2]–[7] shows strong potential for hyperfine WDM multiplexing-demultiplexing. Such hyperfine WDM technology has been used to separate spectral lines from a 12.4-GHz mode-locked laser for applications in photonic arbitrary waveform generation [8] and from a 10-GHz mode-locked laser in order to demonstrate laser repetition rate multiplication [9]. VIPAs have also been used in a Fourier transform pulse shaper geometry [10] to implement novel dispersion compensation systems based on optical signal processing [4], [5]. Recently, we used a direct space-to-time pulse shaper [11] based on the VIPA to demonstrate radio frequency arbitrary waveform generation ($\sim$1 ns time aperture) [12]. Here, for the first time to our knowledge, we report demultiplexing spectra from a VIPA with −3 dB linewidth below 10 pm (1.25 GHz) [13].

Although previous work has demonstrated the potential for high spectral resolution, several publications exhibit clearly asymmetric VIPA passband shapes [2], [14]. In this paper, we have developed a Fresnel diffraction analysis for the passband shape of the VIPA wavelength demultiplexers, which shows that symmetric passbands are possible and identifies the origin of passband asymmetries that are observed. Our theory is validated through experiments. Similar diffraction analyses have been performed for chirped AWG [15], [16]. However, these studies focused on synthesis and broadening of passband shapes, whereas our paper is aimed at implementing filter passbands from the VIPA that are symmetric and as narrow as possible. A Fresnel diffraction analysis has also been reported for the case of grating wavelength demultiplexer with a spatially patterned input beam [11]; however, the emphasis is on the time domain behavior in response to a short pulse input.

The VIPA is a multiple beam interference device that is related to the Lummer-Gehrcke plate and other multiple beam interference devices [17], [18]. The VIPA can be viewed as a modified Fabry–Pérot etalon, and consists of two surfaces. The front (input) surface is coated with an almost 100% reflectivity film except in a window area, which is uncoated or antireflection (AR) coated; the back surface is coated with a partially transmitting film (reflectivity typically $\geq$95%). If the etalon cavity is filled with air, it is called an air-spaced VIPA; otherwise if it is filled with some glass of refractive index $\mathrm{n_r}$, it is called a solid VIPA. Light is input into the device by using a cylindrical lens to focus a collimated laser source through the window area. Due to the high reflectivity of both surfaces of the VIPA etalon, the laser beam experiences multiple reflections back and forth, and the multiple reflections result in multiple diverging output beams. These output beams interfere with each other to form collimated beams with different output angles according to wavelength. The name VIPA comes from the device operating as if there were multiple virtual sources interfering with each other as in a phased array. As in any phased array, the direction of the output beam depends on the phase difference between the array elements (virtual sources). Since this phase difference is frequency dependent, the direction of the output beam also varies with frequency; i.e., the VIPA functions as a spectral disperser (Fig. 1). The VIPA demonstrates several potential advantages over common diffraction gratings: large angular dispersion, low polarization sensitivity, simple structure,

Manuscript received March 9, 2004; revised August 20, 2004. This work was supported in part by the NSF by Grant 0 100 949-ECS and by the ARO by Grant DAAD19-03-1-0275.

S. Xiao and A. M. Weiner are with the School of Electrical and Computer Engineering, Purdue University, West Lafayette, IN 47907 USA (e-mail: sxiao@ecn.purdue.edu;amw@ecn.purdue.edu).

C. Lin is with the Avanex Corp., Fremont, CA 94538 USA (e-mail: Christopher_Lin@avanex.com).

Digital Object Identifier 10.1109/JLT.2005.843531

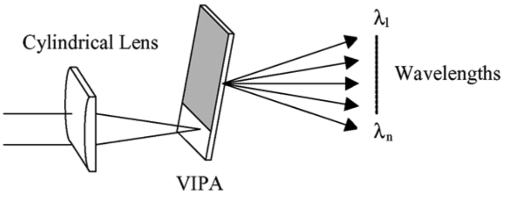

Fig. 1. The VIPA spectral disperser.

potentially low cost, and compactness. For the VIPA spectral disperser, it is important to have a dispersion law to express the angular dispersion quantitatively. Recently, a dispersion law for the VIPA based on plane wave analysis was published by Vega [14]; an improved dispersion law based on paraxial wave analysis has been formulated by Xiao [19]. Here, we present the first paraxial wave theory of the VIPA demultiplexing passband response. Our analysis demonstrates that the symmetry of the passband shape depends on the longitudinal position of the receiver plane [20], which we find to be in good agreement with experimental results. Understanding the passband response allows us to obtain the narrowest linewidth reported to date as well as the first published demonstration of symmetric VIPA passbands.

It is worth comparing briefly with grating demultiplexors, which are commonly observed to exhibit symmetric passbands. For grating demultiplexors, detuning the longitudinal position of the receiver plane leads to broadening, but the passband remains symmetric. It turns out that this is related to the symmetric Gaussian input spatial profile usually found at the grating, as can be ascertained by examining the expressions in [11]. On the other hand, the field directly after a VIPA has a modulated and strongly asymmetric character and a nontrivial spatial phase. An important new result of our work is that the complicated spatial profile immediately after the VIPA does not by itself preclude the possibility of a symmetric passband. However, longitudinal detuning of the receiver plane in conjunction with the asymmetric spatial profile leads both to broadening and to asymmetry.

The remainder of this paper is structured as follows. Section II contains our general theoretical derivation for the demultiplexer passband shape. Section III discusses the linewidth under conditions where it is symmetric. Section IV discusses a spatial chirp effect that arises under conditions where the passband shape becomes asymmetric. Additional discussion is presented in Section V, and we conclude in Section VI.

II. THEORETICAL DERIVATION

The geometry used for our analysis is shown in Fig. 2. An air-spaced VIPA is assumed. The input is assumed to be a Gaussian beam. We consider the multiple reflected spots within the VIPA as arising from a series of virtual sources, each of which has an identical spatial profile, but with different intensities and different transverse and longitudinal source positions. We assumed that the incident beam is focused to a waist with radius w_0 on the back surface of the VIPA, which we further assumed to be located exactly at the front focal plane of the focusing lens of focal length F. According to the geometrical relations in Fig. 2, the nth source has a longitudinal (optical axis z) distance to the thin lens given by $d_n = F + n2t\cos\theta_i$, where $\mathrm{n} = 0$ corresponds to the incident beam. We also ignore any beam reshaping by clipping at the edge of the input window as it is coupled into the VIPA. In our experiment, a well collimated laser source with a beam radius around 1 mm (focal depth $\sim$ several meters) is focused into the VIPA by a cylindrical lens. So a one-dimensional rather than a two-dimensional diffraction analysis is used. The transverse spatial profile of the nth virtual source can be written as

$$E_n(x) = E_0(Rr)^n \exp\left[-\frac{(x - n2t\sin\theta_i)^2}{w_0^2}\right] \tag{1}$$

where R and r are the field reflectivity of the highly and partially reflective surfaces, respectively, w_0 is the focused beam waist radius. The thickness of VIPA etalon is t. θ_i is the incident angle. Note that if the VIPA has a finite aperture of width L, the total number N of sources is limited to $\sim L/[2t\tan(\theta_i)]$. If the aperture is sufficiently large such that the amplitude of the Nth source is small, i.e., $(\mathrm{Rr})^{\mathrm{N}} \ll 1$, then we approximate $\mathrm{N} \rightarrow \infty$ in our later analysis.

A fiber is placed near the back focal plane of the focusing lens to receive a narrow set of the wavelengths which are dispersed due to the spectral dispersion of the VIPA. The distance between the plane where the fiber is placed (the object plane) and the lens is $\mathrm{d}_{\mathrm{obj}}$ in z, which may be detuned from the focal length F.

Starting from a Fresnel diffraction analysis [21], [22], we can derive a general formula which gives the transformation between the input field on the source plane $\mathrm{E}_{\mathrm{in}}(\mathrm{x})$ and the field at the object plane $\mathrm{E}_{\mathrm{out}}(\lambda, \mathrm{x}_{\mathrm{F}})$. Using x_{F} to refer to the lateral position on the object plane, the transformation is written under phase convention $\exp[\mathrm{j}(\omega\mathrm{t} - \mathrm{kz})]$ as

$$\begin{aligned} E_{\mathrm{out}}(\lambda, x_F) \propto{}& \frac{\exp[-ik(d_s - F)]}{\lambda d_s d_{\mathrm{obj}} q} \\ &\times \exp\left[-i\frac{k}{2d_{\mathrm{obj}}}\left(\frac{1}{qd_{\mathrm{obj}}} + 1\right)x_F^2\right] \\ &\times \int E_{\mathrm{in}}(x)\exp\left[-i\frac{k}{2d_s}\left(\frac{1}{qd_s} + 1\right)x^2\right] \\ &\times \exp\left(-i\frac{kx_F x}{qd_s d_{\mathrm{obj}}}\right)dx \end{aligned} \tag{2}$$

where $q = 1/F - 1/d_s - 1/d_{\mathrm{obj}}$ is a parameter, $k = \omega/c = 2\pi/\lambda$ is the propagation constant, d_{s} is the distance between the source plane and the lens, and $\mathrm{d}_{\mathrm{obj}}$ is the distance between the object plane and the lens. Please notice the general transform reduces exactly to a spatial Fourier transform when we have $d_s = d_{\mathrm{obj}} = F$, which means the source plane and object plane match with the front focal plane and back focal plane, respectively. On the other hand, for $\mathrm{q} = 0$, we have an imaging relationship between input and output plane.

The total field at the object plane is the summation of each output field corresponding to the virtual source

$$E_{\mathrm{out}}(\lambda, x_F) = \sum_n E_{\mathrm{out}(n)}(\lambda, x_F) \tag{3}$$

where $\mathrm{E}_{\mathrm{out(n)}}$ is given by (2) where $\mathrm{E}_{\mathrm{in}}(\mathrm{x})$ is replaced by $\mathrm{E}_{\mathrm{n}}(\mathrm{x})$ from (1) and d_{s} is replaced by d_{n}. Then (2) is applied to all of these virtual sources individually.

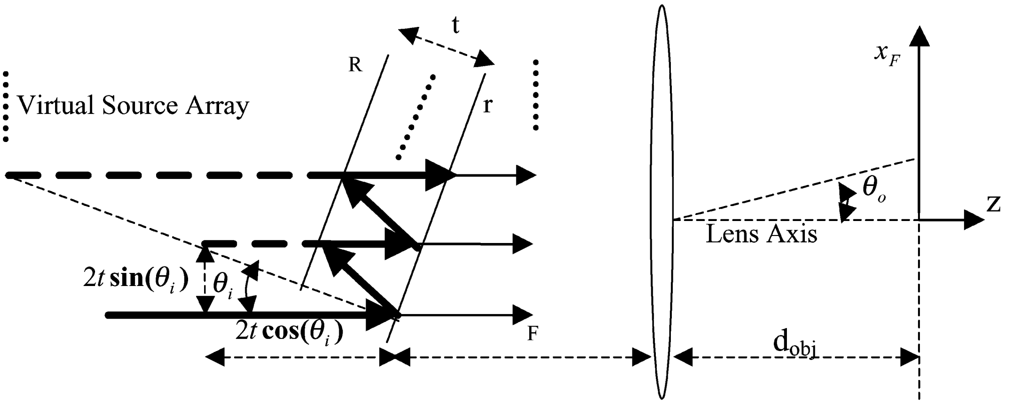

Fig. 2. The VIPA spectral disperser geometry is sketched. The transversal distance and longitudinal distance between neighboring virtual sources are marked in the plot.

To evaluate (2), we will need the formula for the Fourier transform of a chirped Gaussian function

$$\begin{aligned}\int &\exp[-a(x-\Delta)^2]\exp(-ibx^2)\exp(-ik'x)\,dx\\ &=\exp(-ib\Delta^2)\exp(-ik'\Delta)\sqrt{\frac{\pi}{a+ib}}\\ &\quad\times\exp\left[-\frac{(a-ib)(k'+2b\Delta)^2}{4(a^2+b^2)}\right]\end{aligned}\tag{4}$$

where b parameter indicates the chirp of the Gaussian function.

In using (4) to evaluate the contribution from the nth virtual source, we make the following identifications

$$a \leftrightarrow \frac{1}{w_0^2}\tag{5a}$$

$$q_n = \frac{1}{F}-\frac{1}{d_n}-\frac{1}{d_{\text{obj}}}\tag{5b}$$

$$\begin{aligned}b_n &\leftrightarrow \frac{k}{2d_n}\left(1+\frac{1}{q_n d_n}\right)\\ &=\frac{k}{2}\frac{d_{\text{obj}}-F}{d_n d_{\text{obj}}-d_n F-d_{\text{obj}}F}\end{aligned}\tag{5c}$$

$$\Delta_n \leftrightarrow 2nt\sin(\theta_i)\tag{5d}$$

$$k_n' \leftrightarrow \frac{kx_F}{q_n d_n d_{\text{obj}}}\tag{5e}$$

where $\mathrm{b_n}, \Delta_\mathrm{n}, \mathrm{k'_n}$ indicate the quadratic spectral phase, displacement in x and spatial frequency, respectively, corresponding to the nth virtual source according to (2). The spatial frequency concept is similar to that used in optical Fourier transform [21], [22].

To simplify the computation, we assume $\mathrm{a} \gg \mathrm{b_n}$ that indicates a very small quadratic spectral phase for the contributions from each source. This is justified by a brief numerical analysis using typical experimental parameters. According to the expression (5b), for interesting ranges of $\mathrm{d_n}$ and $\mathrm{d_{obj}}$ that are approximately the same as F, $\mathrm{b_n}$ can vanish to zero if and only if $\mathrm{d_{obj}} = \mathrm{F}$. This indicates a strong dependence on $\mathrm{d_{obj}}$ and a weak dependence on $\mathrm{d_n}$ for small $\mathrm{b_n}$ values. The important point is that if there is a slight longitudinal deviation in z of the output object plane from the focal plane, it causes a quadratic phase variation $\exp(-ib_n\Delta_n^2)$ in (2), which is a nonlinear function of the index n. We will be most interested in $\mathrm{d_{obj}} \sim \mathrm{F}$ as we would have substantial line broadening when $|\mathrm{d_{obj}} - \mathrm{F}|$ is greater than or equal to the depth of focus around the back focal plane, as we will see later. The depth of focus is determined by the range of x for which the nth source has appreciable amplitude. The range of x is $\leq$L, where L is the VIPA aperture width, and the focal depth increases as the range of x decreases. The radius of the focused beam waist in the back focal plane after the VIPA is $\mathrm{w_{focal}} = \lambda\mathrm{F/L}$, and the corresponding focal depth is determined by $\pi(\mathrm{w_{focal}})^2/\lambda = \pi\lambda(\mathrm{F/L})^2$. For $\mathrm{L} \sim 10$ mm, $\mathrm{F} \sim 200$ mm, and $\lambda \sim 1.55$ μm, the focal depth $\pi\lambda(\mathrm{F/L})^2$ is $\sim$2 mm, so we require $|\mathrm{d_{obj}} - \mathrm{F}| \leq \pi\lambda(\mathrm{F/L})^2 = 2$ mm. According to these discussions, we have

$$\begin{aligned}|b_n| &= \frac{k}{2}\left|\frac{d_{\text{obj}}-F}{d_n d_{\text{obj}}-d_n F-d_{\text{obj}}F}\right|\\ &\approx \frac{k}{2}\frac{|F-d_{\text{obj}}|}{F^2} \leq \frac{\pi^2}{L^2}.\end{aligned}\tag{6}$$

We have then $|\mathrm{b_n}| \leq 0.1$ mm^{-2}. On the other hand, $a \geq 100$ mm^{-2} since the radius of the beam waist $\mathrm{w_0}$ is $\leq$100 μm under practical conditions. In addition, $\mathrm{b_n}$ is approximately independent of n according to (6), so we drop the subscript n of b in the following analysis. Thus, (4) is reduced to

$$\begin{aligned}\int &\exp[-a(x-\Delta)^2]\exp(-ibx^2)\exp(-ik'x)\,dx\\ &\approx\sqrt{\frac{\pi}{a}}\exp(-ib\Delta^2)\exp(-ik'\Delta)\exp\left(-\frac{(k'+2b\Delta)^2}{4a}\right).\end{aligned}\tag{7}$$

In addition, with $\mathrm{d_{obj}} \approx \mathrm{F}$, we obtain the following approximate expression

$$\begin{aligned}\frac{k}{2d_{\text{obj}}}\left(1+\frac{1}{q_n d_{\text{obj}}}\right) &= \frac{k}{2}\frac{d_n-F}{d_n d_{\text{obj}}-d_n F-d_{\text{obj}}F}\\ &\approx \frac{k(F-d_n)}{2F^2}\end{aligned}\tag{8a}$$

$$d_n d_{\text{obj}} q = \frac{d_n d_{\text{obj}}}{F}-d_n-d_{\text{obj}} \approx -F.\tag{8b}$$

Substituting (8b) into (5e), we obtain $k' \leftrightarrow k_n' = -(kx_F)/(F)$.

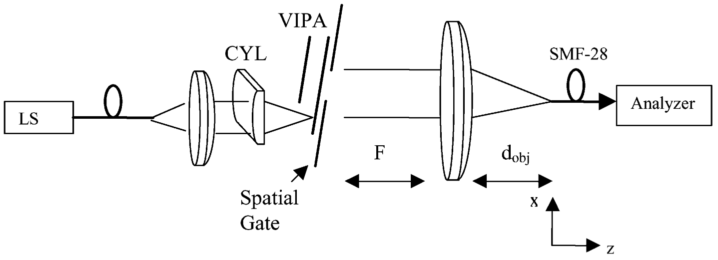

Fig. 3. The experimental setup to test the wavelength demultiplexing filter based on the VIPA. LS: laser source (broadband and tunable are used). CYL: Cylindrical lens. Analyzer: optical spectrum analyzer and power meter are used for broad band source and tunable laser source, respectively.

Substituting (7), (8a) and (8b) into (2), the corresponding output field for the nth source is

$$\begin{aligned} E_{\mathrm{out}(n)} \propto\ & (Rr)^n \exp[-ikn2t\cos(\theta_i)] \exp\left(-ib\Delta_n^2\right) \\ & \times \exp\left(-\frac{(k'+2b\Delta_n)^2}{4a}\right) \exp(-ik'\Delta_n) \\ & \times \exp\left(-i\frac{F-d_n}{2k}(k')^2\right). \end{aligned} \tag{9}$$

The final point to note is that we are focusing on the paraxial region, which is the region with measurable power. For the passband shape discussion here, we will ignore any spatial dependence of the passband shape, i.e., just look at the passband shape on axis at the receiving plane. Since the total transverse shift at the VIPA cannot exceed its aperture L, another approximate relation is

$$\exp\left(-\frac{b^2\Delta_n^2}{a}\right) \geq \exp\left(-\frac{b^2L^2}{a}\right) \approx 1. \tag{10}$$

Thus, we obtain the output field at $x_F = 0$ $(k' = 0)$ is

$$\begin{aligned} & E_{\mathrm{out}}(x_F = 0, \lambda) \\ & \quad \propto \sum_n (Rr)^n \exp[-ikn2t\cos(\theta_i)] \exp[-ib4n^2t^2\sin^2(\theta_i)]. \end{aligned} \tag{11}$$

Equation (11) is the central equation that determines the VIPA demultiplexer transmission spectrum. It consists of three components: the amplitude decay with n, the linear phase, and the quadratic phase.

If there is no quadratic phase term ($\mathrm{b} = 0$ when $\mathrm{d_{obj}} = \mathrm{F}$) in the summation, the transmission spectrum will have a symmetric passband. If b is not zero, the sign of b will decide the direction of passband asymmetry. Both the following experiments and theoretical simulations show that positive $\mathrm{b}(\mathrm{d_{obj}} < \mathrm{F})$ causes an asymmetric tail extending to shorter wavelengths, and negative $\mathrm{b}(\mathrm{d_{obj}} > \mathrm{F})$ causes a tail to longer wavelengths. The passband shape measurement setup is shown in Fig. 3. For now, we ignore the "spatial gate," which is not used at present and will be introduced later. The incident angle is 10°, and the beam waist of the injected beam into the VIPA is $\mathrm{w_o} \sim 24\ \mu$m. The focusing lens after the VIPA has a focal length $\mathrm{F} = 180$ mm. The VIPA has an effective aperture of 7 mm in the x dimension, so the focusing diameter due to the aperture is $\sim$100 μm by $(F\lambda)/L$; for the y transversal dimension, the focusing diameter due to the collimated beam is $\sim$100 μm. A single-mode fiber with a core diameter $\sim$10 μm is used to sample the output field with essentially delta function spatial response. The experimental results and theoretical simulations are shown in Fig. 4. We observe a nice match between our theory and our experiments. This confirms that our approximate derivation is sufficient to describe the main phenomena. Symmetric passband shapes are demonstrated for the appropriate choice of $\mathrm{d_{obj}}$, which we have shown for the first time to our knowledge in the case of VIPA wavelength demultiplexers. Slight longitudinal deviations of the fiber from the back focal plane give rise both to broadening and asymmetry, which may explain the asymmetric passband shapes seen in previous publications [2], [14]. Note that in Fig. 4, the absolute positions of the experimental peaks do not perfectly match the simulation; this can be explained by the fiber translation deviating slightly from the longitudinal z direction in experiments due to imperfect alignments (there is a slight shift in x during the translation in the longitudinal direction, which results in a shift of peak wavelength due to the spectral dispersion function of the VIPA). However, our main interest here is to discuss passband shape, not the peak wavelength position.

III. SPECTRAL LINEWIDTH WITHOUT SPATIAL CHIRP EFFECT

As aforementioned, the demultiplexer transmission spectra have a symmetric passband shape with a minimum spectral linewidth when the receiver is exactly at the back focal plane $(\mathrm{d_{obj}} = \mathrm{F})$. In this case, we have $\mathrm{b} = 0$, for which (9) simplifies to the following:

$$\begin{aligned} E_{\mathrm{out}}(x_F, \lambda) \propto\ & \exp\left(-\pi^2 w_0^2 \frac{x_F^2}{\lambda_0^2 F^2}\right) \\ & \times \sum_{n=0}^{N} \left\{ (Rr)^n \exp\left(-i\frac{4n\pi t\cos(\theta_i)}{\lambda}\right) \right. \\ & \times \exp\left(i\frac{2n\pi t\cos(\theta_i) x_F^2}{\lambda F^2}\right) \\ & \left. \times \exp\left(i\frac{4n\pi t\sin(\theta_i) x_F}{\lambda F}\right) \right\}. \end{aligned} \tag{12}$$

The dependence on both space and wavelength indicates the function of wavelength demultiplexing. Equation (12) gives rise to the VIPA spectral dispersion law, which we have explored in detail elsewhere [19]. The resulting dispersion law based on paraxial wave theory is more accurate than a spectral dispersion law derived previously based on plane wave theory [14].

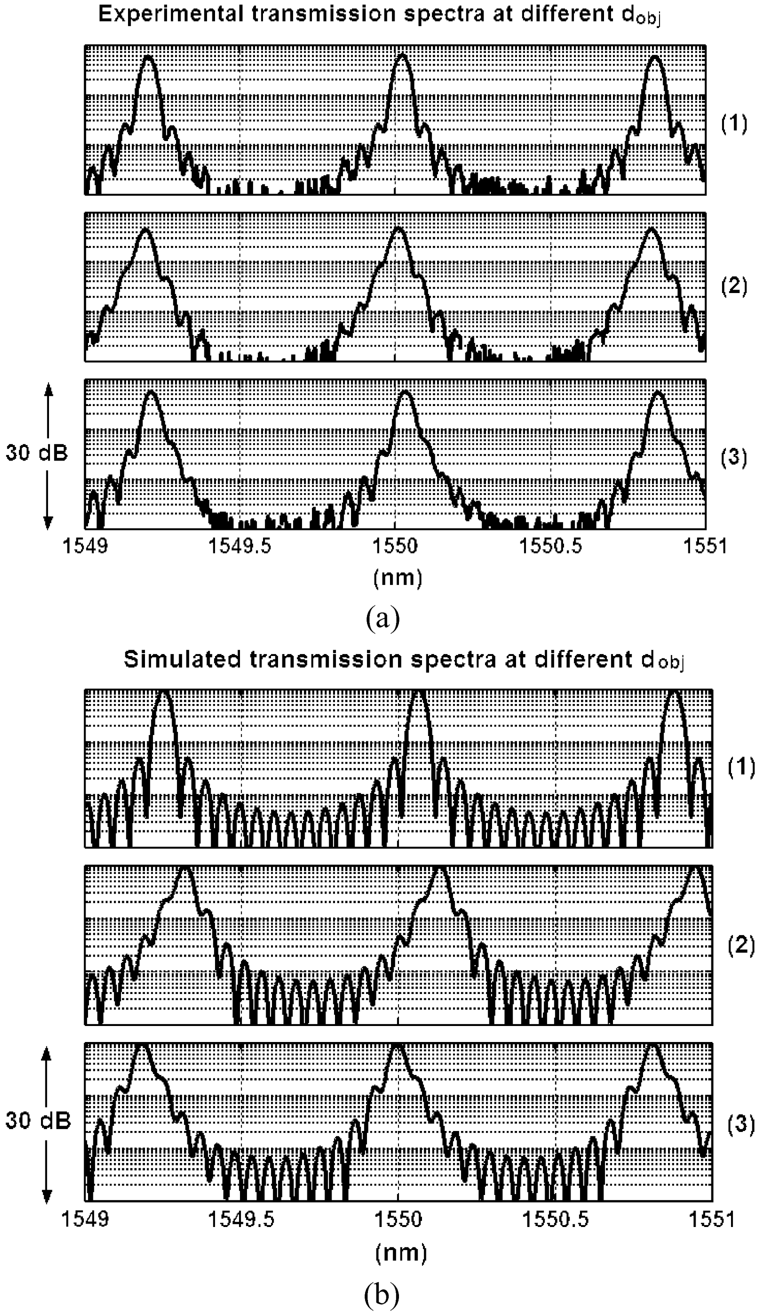

Fig. 4. A comparison between the experimental (a) scanned by the OSA and theoretical (b) transmission spectra . (1), (2), and (3) indicate $\mathrm{d_{obj}} = \mathrm{F}$, $\mathrm{d_{obj}} = \mathrm{F} - 2$ mm, and $\mathrm{d_{obj}} = \mathrm{F} + 2$ mm, respectively. The focusing lens has a focal length $\mathrm{F} = 180$ mm, and the focusing beam radius at the VIPA is $\sim 24\ \mu$m. The VIPA is an air-spaced one with 100 GHz FSR. The incident angle is 10°.

The field at the origin of the back focal plane $(\mathrm{x_F} = 0)$ is

$$E_{\mathrm{out}}(x_F = 0, \lambda) \propto \sum_n (Rr)^n \exp[-ikn2t\cos(\theta_i)]. \qquad (13)$$

The corresponding spectrum expression is

$$I \propto |E|^2 \propto \frac{[1-(Rr)^N] + 4(Rr)^N \sin^2[kNt\cos(\theta_i)]}{(1-Rr)^2 + 4Rr\sin^2[kt\cos(\theta_i)]} \qquad (14)$$

Assuming a large number of interfering beam spots $(\mathrm{Rr})^{\mathrm{N}} \rightarrow 0$, we obtain a spectrum expression with the minimal linewidth

$$I \propto |E|^2 \propto \frac{1}{(1-Rr)^2 + 4Rr\sin^2[kt\cos(\theta_i)]}. \qquad (15)$$

The transmission spectra expression (15) is the same as that of a standard Fabry–Pérot interferometer with the same beam incident angle and the same thickness [18]. Note, however, that the function of the standard Fabry–Pérot and the VIPA are completely different. The standard Fabry–Pérot is a narrow band transmission filter that reflects light outside of the passband, while the VIPA is a spectral disperser that in principle transmits

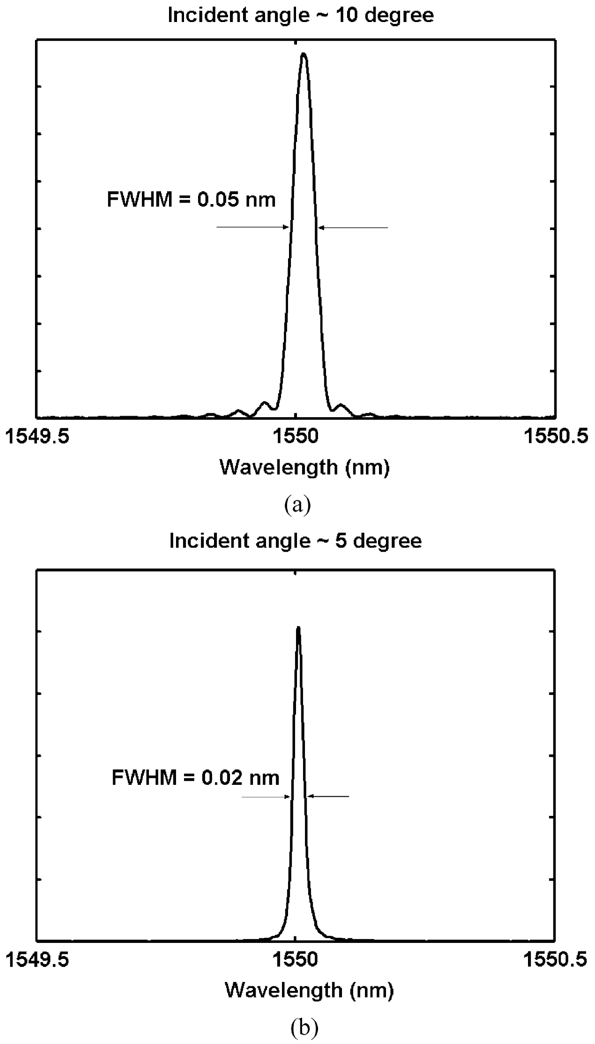

(a)

(b)

Fig. 5. Symmetric passband shapes scanned by the OSA under different incident angles for the air-spaced 100 GHz VIPA. (a) 10°. (b) 5°. $\mathrm{F} = 180$ mm.

all of the light but spreads it to different output angles according to wavelength.

Derived from (15), the theoretically minimal full-width half-maximum (FWHM) or 3-dB transmission bandwidth in frequency and wavelength units is given by

$$\begin{aligned}\mathrm{FWHM}/_{\text{frequency}} &= \frac{c}{2\pi t\cos(\theta_i)}\frac{1-Rr}{\sqrt{Rr}}\\ \mathrm{FWHM}/_{\text{wavelength}} &= \frac{\lambda_0^2}{2\pi\, t\,\cos(\theta_i)}\frac{1-Rr}{\sqrt{Rr}}\end{aligned} \qquad (16)$$

where $m\lambda_0 = 2t\cos(\theta_i)$.

The free spectral range (FSR) is $\mathrm{FSR} = (c)/(2t\cos(\theta_i))$ expressed in frequency units in this case, and the finesse is $\pi\sqrt{Rr}/(1-Rr)$.

An interesting point is that although the spectral dispersion of the VIPA is known to increase with decreasing incident angle [2], [19], the theoretical spectral resolution becomes essentially constant for incident angles small enough that the transverse aperture does not limit the number of reflections. Consider a numerical example: for center wavelength 1550 nm, reflectivity product $\mathrm{Rr} = 95\%$, thickness $\mathrm{t} = 1.5$ mm (100 GHz FSR) and small incident angles with $\cos(\theta_i) \approx 1$, the minimal FWHM is 13 pm (1.625 GHz). For a VIPA with 50 GHz FSR, the minimal FWHM is 6.5 pm assuming the same reflectivity and $\cos(\theta_i) \approx 1$. Spectral resolution can be further improved if a higher Rr is obtained. Please note that there is a slight linewidth dependence on the spatial position according to (12), which we have ignored for simplicity during the above discussion as we are interested in a small range around the zero output angles.

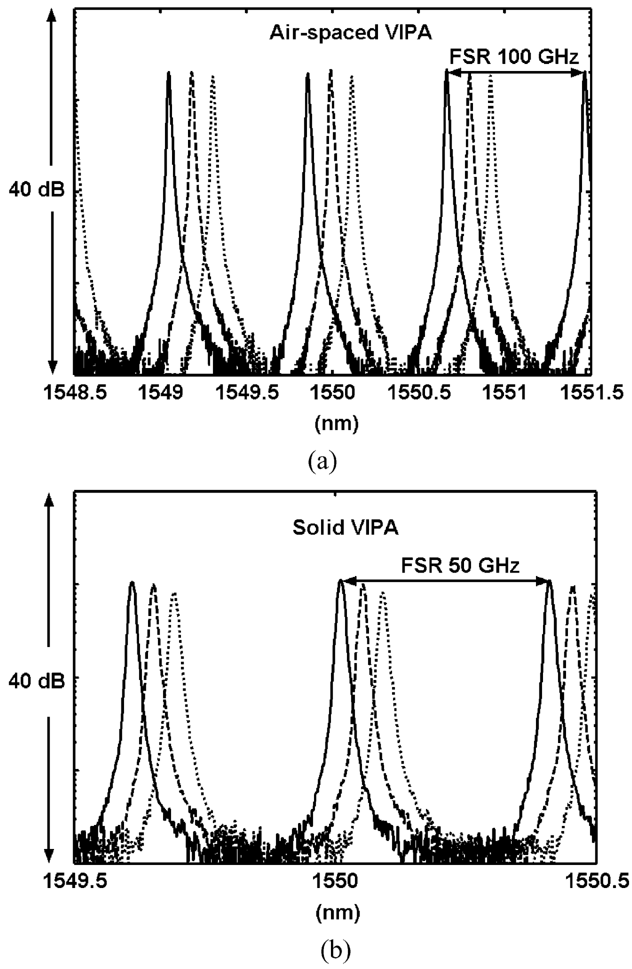

(a)

(b)

Fig. 6. Samples of demultiplexing transmission spectra scanned by the OSA. The test is under the same experimental setup for all VIPAs. $\mathrm{F} = 180$ mm. Incident angles are $\sim 2°$.

An important assumption in such narrow linewidth analysis is the number of interfering beam sources. For a VIPA with a finite aperture ~7 mm, the number of these sources is finite. Consider the following numerical estimation: for an air-spaced VIPA with 100 GHz FSR, thickness ~1.5 mm, $\mathrm{N} \sim 14$ with 10° incident angle, $\mathrm{N} \sim 30$ with 5° incident angle. If incident angles are large ($\sim 10°$), the linewidth can be several times larger than the theoretical minimum. Experimental results are plotted in Fig. 5 to demonstrate the above effect due to a finite number of interfering virtual sources. Clearly, although we obtain symmetric passband shape, we have wide spectra when the incident angle is large. Small incident angle ($<5°$) is the key to obtain narrow spectra for the VIPA with a finite aperture.

Samples of narrow spectra under small incident angle are plotted in Fig. 6 for a 100-GHz FSR air-filled VIPA and

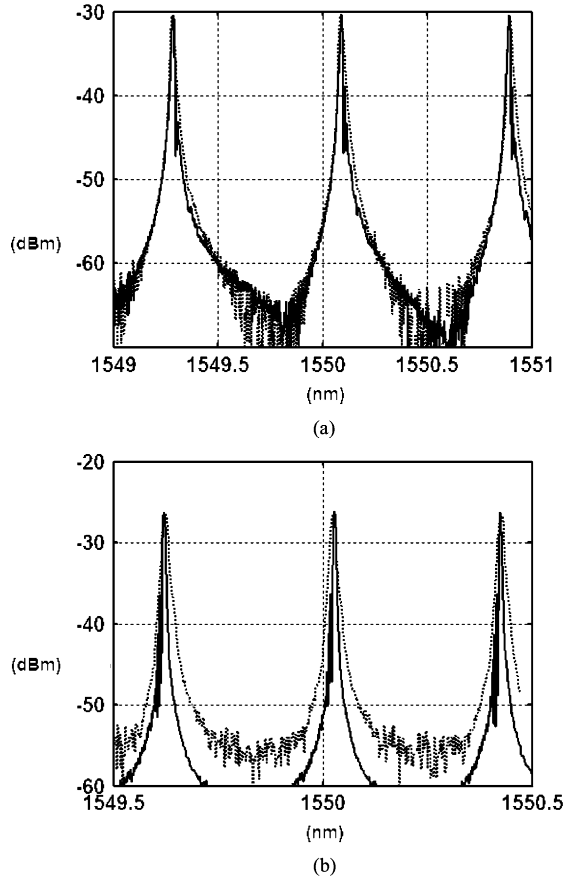

Fig. 7. Transmission spectra samples (solid lines) scanned by the TLS at $\mathrm{F} = 180$ mm. (a) Air-spaced VIPA with 100 GHz FSR. (b) Solid VIPA with 50 GHz FSR. The dashed lines are data ($\mathrm{F} = 180$ mm) scanned by the OSA. Incident angles are $\sim 2^\circ$.

50 GHz-FSR solid VIPA. The line style represents the fiber position, as the receiving fiber translates along x_F uniformly at a step of 0.5 mm. The demultiplexing character is clearly evident. We maintain the same experimental condition (injected beam radius, focusing lens) for both 100 and 50 GHz VIPAs. The incident angle is $\sim 2^\circ$. The 3-dB bandwidths are ~ 18 and ~ 13 pm, respectively, which is comparable to the 10 pm specified resolution of the OSA used in the measurement. Fig. 7 shows the data scanned at a step of 1 pm by a tunable laser source (TLS) with wavelength resolution 0.1 pm (spectral linewidth). The 3-dB bandwidth results are 12 and 7 pm, respectively, which is a result in line with our theoretical prediction. There are some unexpected passband shape distortions in the spectra data from the TLS, which will be discussed in Section V. One remaining issue is that the insertion loss is high (25–30 dB) due to poor coupling into the single-mode fiber receiver, since the focused spot size at the receiving plane is much larger than the fiber mode size. However, this condition allows us to focus on the fundamental limit for the minimal linewidth. Section V mainly discusses the tradeoff between linewidth and coupling loss that occurs as the focused spot size is varied relative to the fiber mode size.

IV. SPATIAL CHIRP EFFECT

For cases when the longitudinal position of the receiving fiber is detuned from the back focal plane, the quadratic phase in the summation (11) contributes to a spatial chirp effect [20], in which the fields at different positions of the VIPA aperture contribute to different center frequencies or wavelengths in the demultiplexing process. This results in asymmetric and broadened passband shapes. An interesting theoretical analysis of the nonlinear quadratic phase effect for $\mathrm{b} \neq 0$ is to look at the contributions from different local virtual sources. To simplify our discussion, Young's double slit interference is used as the basis for our treatment. That is, for a fixed position $\mathrm{x_F} = 0$ in the output plane, we ask at what wavelength two neighboring beam sources will interfere constructively.

Using the demultiplexer passband shape (11), the constructive interference phase matching condition for the nth and $\mathrm{n} + 1$th virtual sources at $\mathrm{x_F} = 0$ is

$$\begin{aligned} &k2t\cos(\theta_i) + 4b[(n+1)^2 - n^2]t^2\sin^2(\theta_i) \\ &\quad = k2t\cos(\theta_i) + 4b(2n+1)t^2\sin^2(\theta_i) = 2m\pi \end{aligned} \tag{17}$$

where

$$b \approx \frac{k}{2}\frac{F - d_{\mathrm{obj}}}{F^2}.$$

From the phase matching condition (17), we can obtain the local demultiplexing wavelength (the wavelength of constructive interference)

$$\lambda = \lambda_0 \left[1 + \frac{(F - d_{\mathrm{obj}})\, t\sin^2(\theta_i)}{F^2\cos(\theta_i)}(2n+1)\right] \tag{18}$$

where $2t\cos(\theta_i) = m\lambda_0$, and λ_0 is the peak output wavelength at the zero output angle.

According to (18), the local demultiplexing wavelength increases or decreases linearly with the index of the virtual sources. The sign of the variation depends on the position of the receiver: increasing for $\mathrm{d_{obj}} < \mathrm{F}$; decreasing for $\mathrm{d_{obj}} > \mathrm{F}$; vanishing for $\mathrm{d_{obj}} = \mathrm{F}$. We name this phenomenon the spatial chirp effect [20].

Since the total number of sources is $(L)/(2t\tan(\theta_i))$, an estimate of the additive wavelength spread due to the spatial chirp effect is

$$\begin{aligned} |\Delta\lambda| &= \lambda_0 \frac{|F - d_{\mathrm{obj}}| t\sin^2(\theta_i)}{F^2\cos(\theta_i)} \times \frac{L}{t\tan(\theta_i)} \\ &= \lambda_0 \frac{L|F - d_{\mathrm{obj}}|}{F^2}\sin(\theta_i). \end{aligned} \tag{19}$$

The spatial chirp effect will strongly broaden and distort the passband shape when the contribution from (19) exceeds the spatial chirp-free linewidth. A numerical value is calculated here: $\mathrm{F} \sim 180$, $\mathrm{L} \sim 7$, $(\mathrm{F} - \mathrm{d_{obj}}) \sim 2$ mm, the incident angle $\sim 10^\circ$. The total wavelength shift is ~ 0.12 nm. Obviously, this will broaden the passband greatly compared to ~ 10 pm FWHM. This wavelength shift vanishes when $\mathrm{d_{obj}} = \mathrm{F}$. Smaller incident angles are helpful to reduce such a passband broadening effect if the receiver's position deviates slightly from the back focal plane of the lens.

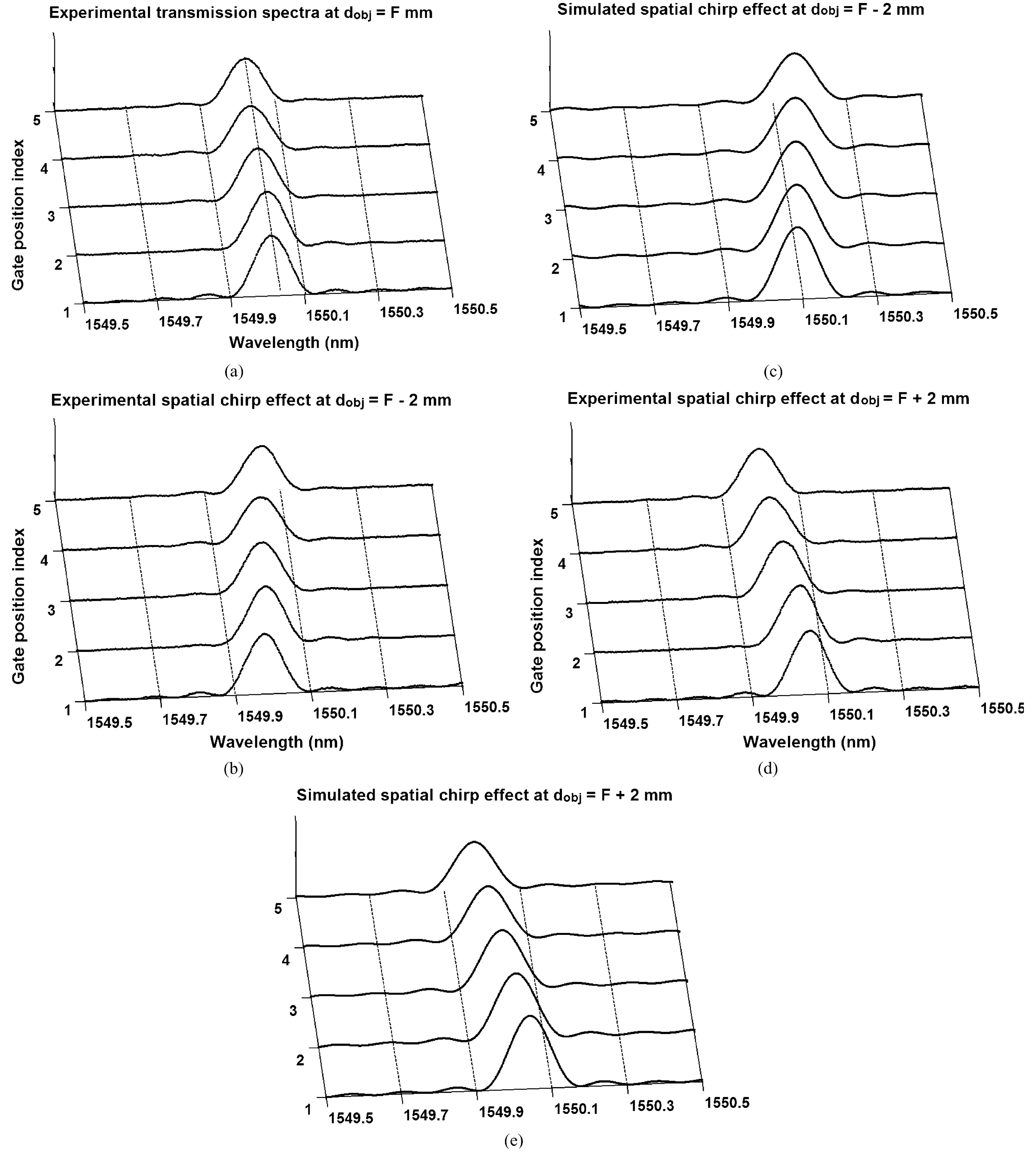

Fig. 8. Transmission spectra with the spatial gate (a)–(e). The gate width is 3 mm, and it is translated uniformly at a step of 1 mm. The VIPA aperture is ~7 mm. $F = 180$ mm. The incident angle is 10°. The gate position index starts from the beam injection side of the air-spaced 100 GHz VIPA.

In order to demonstrate the spatial chirp effect, we introduce a spatial gate (Fig. 3) to look at the spectral contributions from different sets of virtual sources (local demultiplexing). The spatial gate is just a single slit with a certain width, which is made of a pair of razor blades in our setup. This spatial gate allows us to have a closer look at the relation between the spectral asymmetry and the spatial chirp effect. All other conditions are maintained with respect to the experiment in Section III. The 100-GHz air VIPA is used. Measurements are performed with the receiver detuned longitudinally by 2 mm with respect to the position where a symmetric passband shape is observed experimentally, as well as at the symmetric passband position. The data are shown in Fig. 8. The data for the symmetric passband position are shown in Fig. 8(a). The peak position does not depend on the position of the spatial gate at the VIPA output plane; the response is free of spatial chirp, as predicted by our theory. Opposite signs of spatial chirp effect are observed for positive and negative detunings, again, as predicted by our theory. The absolute wavelength shift for the two cases is about 0.05 nm, somewhat smaller than the theory based on Young's double slit interference model. This is reasonable since our spatial gate is not narrow enough to select only two beam spots, and a wider gate is needed in order to have a high signal to noise ratio for the spectra. The experimental spatial-chirp data are in excellent agreement with results from a full simulation that takes into account interference among all of the virtual sources selected by the spatial gate [Fig. 8(c), (e)].

Finally, it is worth remarking on the similarity between this work and previous results on grating-based direct space-to-time pulse shaping [11]. In direct space-to-time pulse shaping, the output pulse in time is a directly scaled version of the spatial pattern imposed onto an ultrashort input pulse. In addition, a longitudinal deviation of the receiving fiber from the back focal plane $\mathrm{d_{obj}} - \mathrm{F}$ gives rise to a multiplicative temporal quadratic phase term. This results in a frequency modulation on top of the shaped intensity profile, which broadens the output spectrum. The spatial chirp effect and passband broadening studied here for the VIPA demultiplexer arise through a similar mechanism. One difference is the asymmetry in the broadened passband shapes observed for the VIPA. This arises through the combination of the spatial chirp effect and the exponentially decaying intensity profile of the virtual sources. In the grating, the diffracted beam profile (without additional spatial patterning) is symmetric, and broadened passband shapes remain symmetric.

V. SPECTRAL LINEWIDTH AND PEAK INSERTION LOSS

In addition to a narrow demultiplexing bandwidth, the insertion loss for the peak wavelength or center channel is also an important performance parameter. In our experiments above, the single-mode fiber receiver with a core diameter $\sim$10 μm acts as a point-like receiver. To reduce insertion loss, we need to match the focused spot size at the receiving plane with the fiber mode. If the fiber mode diameter is much smaller than the focused spot size, we obtained the narrowest linewidth but with a relatively high insertion loss; on the other hand, if the fiber mode diameter is bigger than the focused spot size, we still have a high insertion loss but now with a broadened passband. Although there is a tradeoff between the linewidth and the insertion loss for the single-mode fiber receiver, by matching the focused spot size to the fiber mode, one can obtain the lowest insertion loss at the expense of only a moderate linewidth broadening.

In another experiment, a shorter focal length lens (with $\mathrm{F} = 22$ mm) is used to replace the $\mathrm{F} = 180$ mm lens used previously. This reduces the focused beam diameter to $\sim$10 μm. As a result, the fiber power coupling efficiency is much improved. Examples of the spectra are plotted in Figs. 9 and 10. The passband shape still shows some distortions resolved by the measurement obtained by scanning the tunable laser at a step of 1 pm. For the same air-spaced VIPA with 100 GHz FSR, −1 dB, −3 dB, −20 dB bandwidths are 9, 17 (12 pm for $\mathrm{F} = 180$ mm), 112 pm respectively, and the center channel insertion loss is 10–10.5 dB; for the same solid VIPA with 50 GHz FSR, −1 dB, −3 dB, −20 dB bandwidths are 6, 9 (7 pm for $\mathrm{F} = 180$ mm), 56 pm, respectively, and the center channel insertion loss is 9–9.5 dB. The insertion loss is due to unmatched coupling into fiber and beam clipping at the incident window of the VIPA. The insertion loss may be further improved by using cylindrical lens for independent control of the focusing in the x and y dimensions.

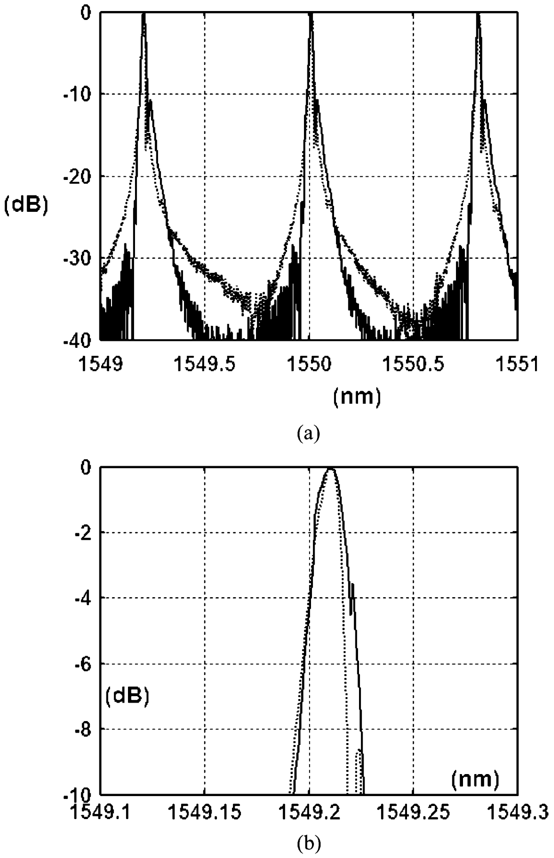

Fig. 9. (a) Transmission spectra samples (solid lines) scanned by the TLS at $\mathrm{F} = 22$ mm for the air-spaced VIPA with 100 GHz FSR (b) is a zoom in. The dashed lines are data scanned by the TLS at $\mathrm{F} = 180$ mm. Incident angles are $\sim 2^\circ$.

One point to be remarked here: the passband shapes from the TLS in Figs. 7, 9, and 10 have some distortions at the level of $\sim$10 dB below from the peak, which are unexpected according to our analysis. These distortions may arise due to aberration effects in the focusing lens, which are resolved by the TLS and are not resolved by the OSA with 10 pm resolution. In addition, the peak mismatch of the TLS data among Figs. 7, 9, and 10 is due to slight variations $(\leq 0.1^\circ)$ of the incident angles.

The insertion loss of a VIPA demultiplexer has been discussed in [2], [3] using numerical simulations. There are three basic contributions to the insertion loss: beam clipping at the input to the VIPA as small as a few percent loss [3], diffraction into multiple orders [3], [23] (as small as $\sim$1 dB [3]) and mode coupling [3]. We would like here to analyze the mode coupling efficiency based on our theory discussed in previous sections. The mode of a standard single-mode fiber is Gaussian, and the power coupling efficiency is determined by the field overlap integral. To optimize the efficiency, we suggest two cylindrical

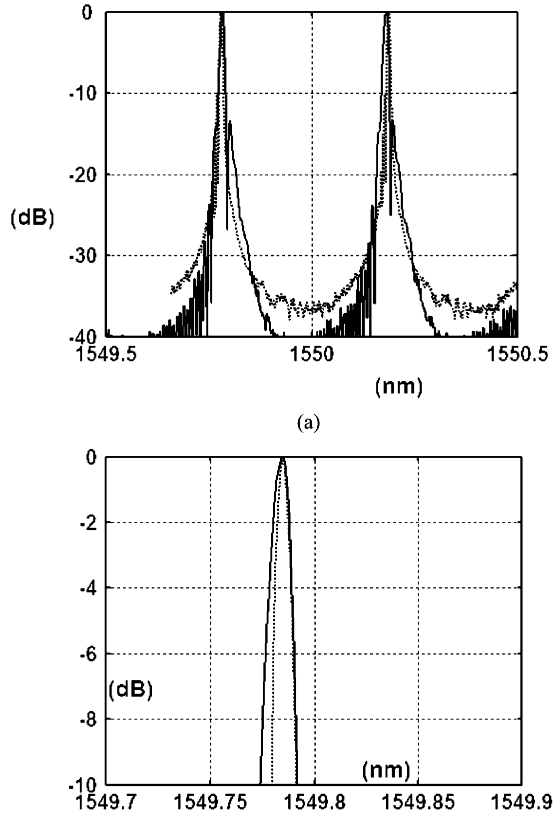

Fig. 10. (a) Transmission spectra samples (solid lines) scanned by the TLS at $F = 22$ mm for the solid VIPA with 50 GHz FSR (b) zoom in. The dashed lines are data scanned by the TLS at $F = 180$ mm. Incident angles are $\sim 2^\circ$.

lenses with common back focal plane to focus in the transversal directions x and y separately, instead of one spherical lens. According to (12), including also the dependence on y, the output field at the back focal plane is shown in (20) at the bottom of the page, where F, f are the focal lengths of the two cylindrical lens focusing in x and y, respectively, and W is the input collimated beam to the VIPA in y radius assuming a Gaussian profile, and for simplicity, x_F is replaced with x. The mode expression of single-mode fibers is a Gaussian function [24]

$$E_0(x,y) \propto \exp\left(-\frac{x^2}{a^2}\right)\exp\left(-\frac{y^2}{a^2}\right) \tag{21}$$

where a is the mode radius of the single-mode fiber.

In (20), the first term gives the amplitudes of the different diffraction orders. This first term is slowly varying relative to the focused spot of any single order (determined by the third term). Therefore, the first term has little effect on the mode coupling calculation and is ignored. For small incident angles, i.e., $\theta_i \sim 2^\circ$ for our parameters, the insertion loss into higher diffraction order is small (≤ 1 dB in our case) [3]. We take the wavelength peak at the origin ($x = y = 0$) without loss of generality, which means $2t\cos(\theta_i) = m\lambda$, where m is an integer. The mode in the y dimension can be perfectly matched according to (20) when the focus in y satisfies $a = \lambda f/(\pi W)$. All we need to consider is the mode coupling in the x dimension. The dependence of the output field on x is

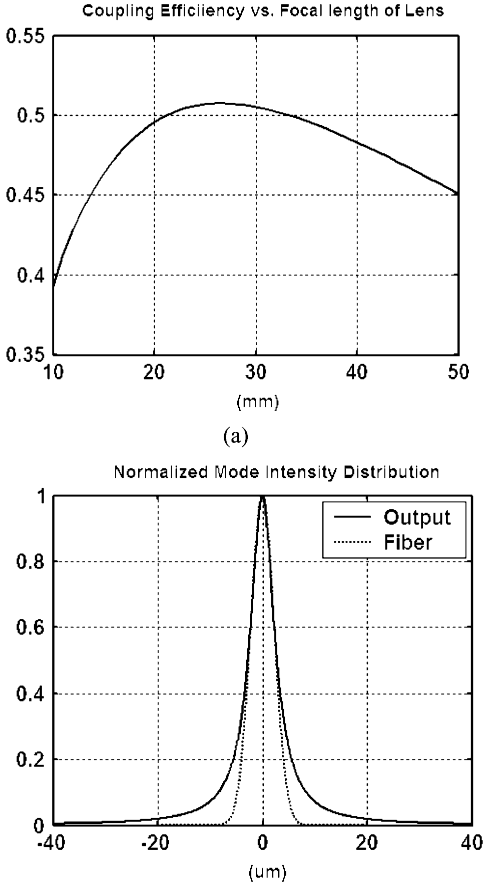

Fig. 11. (a) Power coupling efficiency varies with focal length F of focusing cylindrical lens in x. A perfect match assumed in y with $f = 11$ mm. (b) Corresponding mode intensity distribution when maximum efficiency achieved at $F = 26$ mm.

$$E_{\text{out}}(x,\lambda) \propto \frac{1}{1 - Rr\exp\left(i\frac{4\pi t\sin(\theta_i)x}{\lambda F} + i\frac{2\pi t\cos(\theta_i)x^2}{\lambda F^2}\right)}. \tag{22}$$

$$E_{\text{out}}(x,y,\lambda) \propto \exp\left(-\pi^2 w_0^2\frac{x^2}{\lambda^2F^2}\right)\times\exp\left(-\pi^2W^2\frac{y^2}{\lambda^2f^2}\right) \times\frac{1}{1 - Rr\exp\left(-i\frac{4\pi t\cos(\theta_i)}{\lambda} + i\frac{4\pi t\sin(\theta_i)x}{\lambda F} + i\frac{2\pi t\cos(\theta_i)x^2}{\lambda F^2}\right)} \tag{20}$$

According to (22), the output field in space is not exactly Lorentzian even without the second spatial quadratic phase term. This differs from the assumption of a lorentzian shape [2], [3], therefore, we can expect the coupling efficiency to deviate from the estimate in [2], [3].

The power coupling efficiency between two modes is given by

$$\eta = \frac{\left|\int E_{\mathrm{out}}(x,\lambda)E_0(x)\,dx\right|^2}{\int |E_{\mathrm{out}}(x,\lambda)|^2\,dx \int |E_0(x)|^2\,dx} \tag{23}$$

where $\mathrm{E_0(x)}$ and $\mathrm{E_{out}(x,\lambda)}$ are given by (21) and (22), respectively. It is interesting to show a numerical simulation. In our case, we take thickness $\mathrm{t} = 1.5$ mm, reflectivity product $\mathrm{Rr} = 0.95$, wavelength $\lambda = 1.55\mu$m, and fiber mode radius $\mathrm{a} = 4.5\mu$m. The incident angle θ_{i} is $\sim 2.24°$, chosen to satisfy $2\mathrm{t}\cos(\theta_{\mathrm{i}}) = \mathrm{m}\lambda$ (m is an integer). A simulation result in plotted in Fig. 11. The total maximum power coupling efficiency is about 50% according to our simulations when $\mathrm{F} = 26$ mm. Thus, there is a 3-dB loss due to the fundamental mode mismatch, which is higher than the $\sim$1 dB coupling loss reported in [2] and [3], where the lorentzian mode approximation was used. The total loss for the VIPA demultiplexer results fundamentally from this mode coupling loss, diffraction into multiple orders and beam clipping at the input to the VIPA as well as any excess loss associated with imperfect optical components.

VI. CONCLUSION

We have analyzed the behavior of the passband of the VIPA demultiplexer and have shown that either symmetric or asymmetric passband shapes can be obtained depending on longitudinal position of the receiver. We have also shown that the asymmetric passband shapes have wider linewidth than the symmetric passband shape. We identify a spatial chirp effect strongly related to the passband asymmetry. Small incident angle is useful in minimizing the spatial chirp effect and also increases the number of interfering virtual sources for the VIPA with finite aperture, resulting in a smooth passband shape with narrow linewidth. Based on our analysis results, we have been able to demonstrate VIPA demultiplexers with symmetric passband shapes, $\sim$10 pm (1.25 GHz) -3 dB transmission bandwidths, and 9–10 dB insertion loss; which make the VIPA a promising candidate as a spectral disperser for Hyperfine WDM.

REFERENCES

[1] K. Takada, M. Abe, T. Shibata, and K. Okamoto, "10-GHz-spaced 1010-channel tandem AWG filter consisting of one primary and ten secondary AWGs," *IEEE Photon. Technol. Lett.*, vol. 13, no. 6, pp. 577–578, 2001.

[2] M. Shirasaki, "Large angular dispersion by a virtually imaged phased array and its application to a wavelength demultiplexer," *Opt. Lett.*, vol. 21, pp. 366–368, 1996.

[3] M. Shirasaki, A. N. Akhter, and C. Lin, "Virtually imaged phased array with graded reflectivity," *IEEE Photon. Technol. Lett.*, vol. 11, pp. 1443–1445, 1999.

[4] M. Shirasaki, "Chromatic-dispersion compensator using virtually imaged phased array," *IEEE Photon. Technol. Lett.*, vol. 9, pp. 1598–1560, 1997.

[5] ——, "Compensation of chromatic dispersion and dispersion slope using a virtually imaged phased array," in *Opt. Fiber Commun. Conf. TuS1-3*, 2001.

[6] ——, "Virtually imaged phased array (VIPA) having air between reflecting surfaces," Patent 5 969 866, Oct. 19, 1999.

[7] ——, "Optical apparatus which uses a virtually imaged phased array to produce chromatic dispersion," Pub. US 20030021046, Jan. 30, 2003.

[8] T. Yilmaz, C. M. DePriest, T. Turpin, J. H. Abeles, and P. J. Delfyett, "Toward a photonic arbitrary waveform generator using a modelocked external cavity semiconductor laser," *IEEE Photon. Technol. Lett.*, vol. 14, no. 11, pp. 1608–1610, 2002.

[9] M. Currie, F. K. Fatemi, and J. W. Lou, "Increasing laser repetition rate by spectral elimination," in *CThPDA8, Conf. Laser and Electro Optics*, Baltimore, MD, Jun. 1–6, 2003.

[10] A. M. Weiner, "Femtosecond pulse shaping using spatial light modulators," *Rev. Sci. Instrum.*, vol. 71, no. 5, pp. 1929–1960, 2000.

[11] D. E. Leaird and A. M. Weiner, "Femtosecond direct space-to-time pulse shaping," *IEEE J. Quantum Electron.*, vol. 37, no. 4, pp. 494–504, 2001.

[12] S. Xiao, J. D. McKinney, and A. M. Weiner, "Photonic microwave arbitrary waveform generation using a virtually-imaged phased-array (VIPA) direct space-to-time pulse shaper," *IEEE Photon. Technol. Lett.*, vol. 16, pp. 1936–1938, 2004.

[13] S. Xiao, A. M. Weiner, and C. Lin, "Demultiplexers with 10 pm (1.25 GHz) -3 dB transmission bandwidth using a virtually imaged phased array (VIPA)," in *TuL1, Optical Fiber Commun. Conf.*, Los Angeles, CA, Feb. 22–27, 2004.

[14] A. Vega, A. M. Weiner, and C. Lin, "Generalized grating equation for virtually-imaged phased-array spectral dispersers," *Appl. Opt.*, vol. 42, pp. 4152–4155, 2003.

[15] M. C. Parker and S. D. Walker, "Design of AWG's using hybrid Fourier-Fresnel transform techniques," in *J. Sel. Topics Quantum Electron.*, vol. 6, 1999, pp. 1379–1384.

[16] ——, "A Fourier-Fresnel integral-based transfer function model for a near-parabolic phase-profile arrayed-waveguide grating," *IEEE Photon. Technol. Lett.*, vol. 11, pp. 1018–1020, 1999.

[17] O. Lummer and E. Gehrcke, *Ann. D. Physik*, vol. 10, pp. 457–477, 1903.

[18] M. Born and E. Wolf, *Principles of Optics*. Cambridge, U.K.: Cambridge University, 1999, pp. 359–386.

[19] S. Xiao, A. M. Weiner, and C. Lin, "A dispersion law for virtually-imaged phased-array based on paraxial wave theory," *IEEE J. Quantum Electron.*, vol. 40, no. 4, pp. 420–426, 2004.

[20] ——, "Spatial chirp effect in virtually-imaged phased-array wavelength demultiplexers," in *CWP6, Conf. Lasers Electro Opt.*, Baltimore, MD, Jun. 1–6, 2003.

[21] J. W. Goodman, *Introduction to Fourier Optics*. San Francisco, CA: McGraw-Hill, 1968, pp. 77–96.

[22] H. A. Haus, *Waves and Fields in Optoelectronics*. Englewood Cliffs, NJ: Prentice-Hall, 1984, pp. 81–107.

[23] L. Yang, "Analytical treatment of virtual image phase array," in *WS3, Optical Fiber Commun. Conf.*, Anaheim, CA, Mar. 17–22, 2002.

[24] D. Marcuse, "Gaussian approximation of the fundamental modes of graded-index fibers," *J. Opt. Soc. Amer.*, vol. 68, pp. 103–109, 1978.

Shijun Xiao (S'03) was born in Chengdu, China, in 1979. He received the B.S. degree in electronics from Beijing University, Beijing, China, in 2001, and the M.S.E.C.E. degree in electrical and computer engineering from Purdue University, West Lafayette, IN, in 2003.

He is currently pursuing the Ph.D. degree in electrical and computer engineering at Purdue University. His current research area includes optical signal processing and pulse shaping, optical hyperfine-WDM/subcarrier multiplexing (SCM) communications, and radio frequency (RF)/microwave photonics.

Mr. Xiao is a student member of the IEEE Lasers and Electro-Optics Society and the Optical Society of America (OSA). He received the Andrews Fellowship from Purdue University for two years. He received the IEEE LEOS Graduate Student Fellowship in 2004.

Andrew M. Weiner (S'84–M'84–F'95) received the Sc.D. degree in electrical engineering from the Massachusetts Institute of Technology (MIT), Cambridge, in 1984.

From 1979 through 1984, he was a Fannie and John Hertz Foundation Graduate Fellow at MIT. In 1984, he joined Bellcore, at that time one of the premier research organizations in the telecommunications industry. In 1989, he was promoted to Manager of Ultrafast Optics and Optical Signal Processing. He moved to Purdue University in 1992 as Professor of Electrical and Computer Engineering, and is currently the Scifres Distinguished Professor of Electrical and Computer Engineering. From 1997 to 2003 he served as as ECE Director of Graduate Admissions. His research focuses on ultrafast optical signal processing and high-speed optical communications. He is especially well known for pioneering the field of femtosecond pulse shaping, which enables generation of nearly arbitrary ultrafast optical waveforms according to user specification. He has published four book chapters and more than 120 journal articles. He has been author or coauthor of over 200 conference papers, including approximately 60 conference invited talks, and has presented over 50 additional invited seminars at universities or industry. He holds five U.S. patents.

Prof. Weiner has received numerous awards for his research, including the Hertz Foundation Doctoral Thesis Prize (1984), the Adolph Lomb Medal of the Optical Society of America (1990), awarded for pioneering contributions to the field of optics made before the age of thirty, the Curtis McGraw Research Award of the American Society of Engineering Education (1997), the International Commission on Optics Prize (1997), the IEEE LEOS William Streifer Scientific Achievement Award (1999), the Alexander von Humboldt Foundation Research Award for Senior U.S. Scientists (2000), and the inaugural Research Excellence Award from the Schools of Engineering at Purdue (2003). He is a Fellow of the Optical Society of America. He has served on or chaired numerous research review panels, professional society award committees, and conference program committees. During 1988–1989, he served as an IEEE Lasers and Electro-optics Society (LEOS) Distinguished Lecturer. He was General Co-Chair of the 1998 Conference on Lasers and Electro-optics, Chair of the 1999 Gordon Conference on Nonlinear Optics and Lasers, and Program Co-chair of the 2002 International Conference on Ultrafast Phenomena. In addition, he has served as Associate Editor for the IEEE JOURNAL OF QUANTUM ELECTRONICS, IEEE PHOTONICS TECHNOLOGY LETTERS, and *Optics Letters*. He served as an elected member of the Board of Governors of IEEE LEOS from 1997–1999 and as Secretary/Treasurer of IEEE LEOS from 2000–2002. He is currently a Vice President (representing IEEE LEOS) of the International Commission on Optics (ICO).

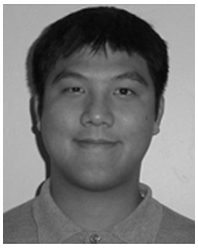

Christopher Lin received the B.S. and M.Eng. degrees in electrical engineering and computer science and the B.S. degree in economics from the Massachusetts Institute of Technology, Cambridge, in 2000.

Since graduating, he has been with Avanex Corporation, Fremont, CA, where he is currently a Product Development Manager. He has worked on the design and simulation of passive optical components for optical communications systems including multiplexers, interleavers, and chromatic dispersion compensators.